Catalysis Science & Technology

Accepted Manuscript

This article can be cited before page numbers have been issued, to do this please use: Y. Xia, P. Wang, X. Wang, F. Chen and H. Yu, *Catal. Sci. Technol.*, 2025, DOI: 10.1039/D5CY00838G.

ROYAL SOCIETY OF CHEMISTRY

rsc.li/catalysis

View Article Online
DOI: 10.1039/D5CY00838G

ARTICLE

Directional Electron Transfer from CoS_2 to Mo_2C for Weakened Mo-H Bond Toward Boosting Photocatalytic H_2 Production

Received 00th January 20xx,
Accepted 00th January 20xx

DOI: 10.1039/x0xx00000x

Youran Xia[a], Ping Wang[a,*], Xuefei Wang [a], Feng Chen [a], Huogen Yu[a,b,*]

Molybdenum carbide (Mo_2C) has been regarded as a potential cocatalyst for boosting the photocatalytic hydrogen-generation performance of photocatalysts owing to its unique Pt-mimetic electronic structure, which arises from the hybridization between Mo-4d and C-s/p orbitals. However, the overpowered Mo-H bonding promotes favorable H^+ adsorption while hindering hydrogen desorption, thereby restricting its practical application in hydrogen evolution reactions (HER). In this paper, the strategy of constructing a CoS_2-Mo_2C heterojunction leverages directional electron transfer from CoS_2 to Mo_2C to enhance the occupancy of antibonding orbitals at Mo sites for weakening Mo-H_{ads} bonds and significantly improving hydrogen-evolution activity. Herein, the CoS_2-Mo_2C heterojunction is successfully fabricated via a two-step calcination method, and then integrated with TiO_2 through ultrasonic assistance to fabricate the CoS_2-Mo_2C/TiO_2 photocatalyst. The optimized CoS_2-Mo_2C/TiO_2 photocatalyst exhibits outstanding photocatalytic activity with a hydrogen-generation rate of 1964.53 μmol h^{-1} g^{-1}, which is ca. 15.1 and 2.6-fold higher than that of pristine TiO_2 and Mo_2C/TiO_2, respectively. Experimental characterizations and DFT calculations reveal that the antibonding orbital occupancy of Mo sites increases by the electron transfer from CoS_2 to Mo_2C in the CoS_2-Mo_2C heterojunction, leading to the weakened Mo-H_{ads} bond from 2.025 Å in Mo_2C to 1.976 Å in CoS_2-Mo_2C. This study proposes crucial design principles for Mo_2C-based heterojunction cocatalysts, fostering the advancement of sustainable hydrogen-production technologies.

1. Introduction

Photocatalytic hydrogen production via semiconductor materials presents a sustainable strategy to concurrently tackle global energy crises and environmental issues through solar energy conversion.[1-6] Among candidates, TiO_2 have undergone extensive investigation due to their unparalleled chemical durability, thermal stability, and biocompatibility.[7-11] However, their practical implementation is critically hindered by ultrafast charge-carrier recombination and sluggish hydrogen evolution kinetics, which collectively restrict the solar-to-hydrogen efficiency to <0.5% in most unmodified TiO_2.[12-14] Cocatalyst modification has emerged as a cornerstone strategy to accelerate photocatalytic hydrogen evolution performance, concurrently enabling ultrafast photogenerated electron transfer and active site engineering.[15-19] To date, noble metals (e.g. Pt,[20] Au,[21-23] Pd,[24] Rh[25]) have long been established as highly efficient cocatalysts for boosting photocatalytic performance, leveraging their exceptional electron conductivity to facilitate rapid charge transfer. Notably, the commercial viability of these noble metal-based systems is critically constrained by their exorbitant costs. This has spurred intensive research into non-precious transition metal compounds, including phosphides,[26-28] carbides,[29-31] and sulfides,[32-35] which offer comparable photocatalytic enhancements at a fraction of the cost. Molybdenum carbide (Mo_2C) stands out as a prototypical non-precious metal cocatalyst for photocatalytic H_2 production with Pt-like catalytic properties, which is attributed to the unique hybridization of Mo 4d orbitals and C s/p orbitals.[36-38] Studies have shown that the hydrogen-evolution activity of Mo_2C is primarily governed by its exposed Mo active sites, which serve as prime catalytic centers for hydrogen intermediate management. Specifically, these sites enable efficient adsorption and activation of hydrogen species (H*) through the formation of Mo-H_{ads} surface intermediates, a process critical for overcoming the kinetic barriers in hydrogen evolution.[39] However, Mo_2C features strong Mo-H bonds (65-75 kcal mol^{-1}) for efficient hydrogen evolution while Pt-H bonds exhibit an optimal dissociation energy of 60 kcal mol^{-1},[40] leading to excessive hydrogen adsorption that hinders H_2 desorption from active Mo sites (Fig. 1A-(1)). This thermodynamic mismatch creates a kinetic bottleneck in the hydrogen-evolution reaction, as the energy barrier for H_2 desorption exceeds the optimal range for rapid turnover. Therefore, developing effective strategies to modulate the Mo-H bond strength and optimize the electronic structure of Mo_2C is critical for enhancing photocatalytic activity.

Extensive research has demonstrated that metal coupling,[41-43] heteroatom doping,[44, 45] and heterojunction engineering[46] effectively weaken Mo-H bonds by modulating the electronic structure of Mo active sites. For instance, Xu *et al*. demonstrate that interfacial engineering of Mo_2C with Ni, Co, or Fe optimizes Mo-H bonding energy into an ideal range for hydrogen desorption, consequently

[a.] *School of Chemistry, Chemical Engineering and Life Sciences, Wuhan University of Technology, Wuhan, 430070, PR China*
[b.] *Laboratory of Solar Fuel, Faculty of Materials Science and Chemistry, China University of Geosciences, Wuhan, 430078, PR China*
†Electronic Supplementary Information (ESI) available. See DOI: 10.1039/x0xx00000x

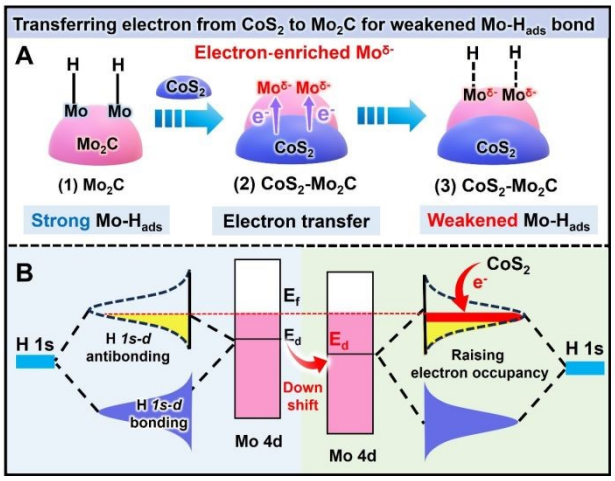

Fig. 1. (A) Schematic diagram for weakening Mo-H_{ads} bond in CoS_2-Mo_2C heterojunction: (1) Mo_2C with strong Mo-H_{ads} bond; (2) Electron transfer from CoS_2 to Mo_2C: (3) Weakened Mo-H_{ads} bond in CoS_2-Mo_2C heterojunction. (B) Schematic diagram for electron transfer from CoS_2 to Mo_2C to raise the antibonding-orbital occupancy of Mo site for weakened Mo-H_{ads} bond.

enhancing the intrinsic catalytic performance for hydrogen evolution.[42] Similarly, Wang et al. pioneer the synthesis of B, N co-doped Mo_2C via microwave plasma chemical vapor deposition (MPCVD), where the optimized charge transfer between H* and Mo_2C reduces hydrogen binding energy, enabling efficient and stable hydrogen evolution across diverse environments.[44] Luo et al. further harnessed chemical coupling in CoP-Mo2C heterojunctions to induce electron migration from CoP to Mo sites to weaken Mo-H bonds and accelerate HER kinetics.[46] In our prior works, constructing WC/Mo_2C and MoS_2/Mo_2C heterojunctions modulated the d-band center of Mo_2C, effectively reducing Mo-H bond strength and achieving obvious enhancement in photocatalytic hydrogen-production performance of TiO_2.[38,47] Collectively, these studies highlight that strategies such as heterojunction engineering enable precise regulation of Mo-H adsorption strength as a critical parameter for optimizing HER activity. However, the underlying theoretical framework remains insufficiently developed to offer tangible guidance for future research. This knowledge gap is primarily attributed to the lack of systematic studies on the correlation between electronic structure modulation and Mo-H bond energetics and insufficient atomistic insights into interfacial charge transfer dynamics in heterojunction systems. Addressing these gaps requires integrating advanced computational approaches to unravel the mechanistic linkages between structural engineering and catalytic efficiency.

Typically, the intensity of Mo-H bonds is intrinsically determined by antibonding orbital occupancy, which originates from Mo 4d and H 1s orbital hybridization. Based on molecular orbital theory, bonding orbitals are fully occupied at lower energy levels, while antibonding orbitals form at higher energies with partial electron occupancy. When H is adsorbed onto the active Mo site of Mo_2C, the intensity of Mo-H bonds in Mo_2C is inherently linked to the low occupancy of antibonding orbitals at higher energies, which stabilizes the Mo-H interaction to form strong Mo-H bonds (Fig. 1B left). Hence, engineering electron-rich environments around Mo sites emerges as an efficient strategy to increase antibonding orbital occupancy, thus weakening Mo-H_{ads} bonds and optimizing hydrogen-production efficiency. In this work, the strategy of constructing a CoS_2-Mo_2C heterojunction by directional electron transfer from electron-donating CoS_2 to Mo_2C is achieved (Fig. 1A-(2)), populating the Mo d-orbitals to create electron-rich active sites. This electronic modulation increases antibonding orbital occupancy in Mo, thus weakening the strength of Mo-H bonds and enhancing the H_2-generation activity of Mo_2C (Fig. 1A-(3) and Fig. 1B-right). The CoS_2-Mo_2C heterojunction was synthesized via a molten salt method, where CoS_2 nanosheets were grown on Mo_2C surfaces, followed by ultrasonic-assisted integration with TiO_2 to form the CoS_2-Mo_2C/TiO_2 composite. Photocatalytic measurements demonstrate that the introduction of CoS_2 leads to a significant increase in hydrogen evolution rate compared to pristine TiO_2 and Mo_2C/TiO_2. XPS results and density functional theory (DFT) calculations show that the present d-orbital electron strategy of constructing CoS_2-Mo_2C heterojunction by CoS_2-mediated charge transfer raises antibonding orbital occupancy of Mo sites and destabilizes Mo-Hads bonds. These results provide a novel approach for designing high-performance Mo_2C-based heterojunction cocatalysts in photocatalytic H_2 generation.

2. Experimental

2.1. Synthesis of the Porous Mo_2C.

Porous Mo_2C is synthesized via a molten salt method using potassium chloride as a template. The mixture of $(NH)_6Mo_7O_{24}{\cdot}4H_2O$, melamine, and KCl (20 g) is calcined to 800 °C (5 °C min^{-1}) and maintained for 6 h in a quartz tube furnace under N_2 atmosphere. After cooling to room temperature, the final black powder named Mo_2C undergoes washing with deionized water to remove residual KCl and drying in a 60 ℃ oven.

2.2 Synthesis of CoS_2-Mo_2C heterojunction.

The CoS_2-Mo_2C heterojunction is synthesized by a calcination strategy, thoroughly grinding the above Mo_2C, KSCN (10 g), and $CoCl_2{\cdot}6H_2O$ for 5 minutes and heating to 380 ℃ (5 ℃ min^{-1}, air atmosphere) for 2 h. After cooling to room temperature, the calcined materials are washed with deionized water for three times, then put in a 60 °C oven to dry. To investigate the mass effect of CoS_2 on Mo_2C, the theoretical weight ratios of CoS_2 to Mo_2C are set as 2, 6,10, 16, and 20 wt%. The corresponding materials are marked as CoS_2-Mo_2C(X wt%) (here, X represents the mass ratio of CoS_2 to Mo_2C).

2.3. Synthesis of CoS_2-Mo_2C/TiO_2 photocatalysts.

The CoS_2-Mo_2C/TiO_2 composite photocatalysts are synthesized via ultrasonic dispersion in 25 vol% ethanol solution. CoS_2-Mo_2C and TiO_2 are ultrasonically dispersed in an ethanol solution with a volume ratio of 25% for 30 minutes. According to the name rule of CoS_2-Mo_2C(X wt%), the corresponding materials are denoted as CoS_2-Mo_2C(X wt%)/TiO_2 (here, X is the weight ratio of CoS_2 to Mo_2C). Moreover, the mass ratio of CoS_2-Mo_2C to TiO_2 in CoS_2-Mo_2C(X wt%)/TiO_2 is controlled to be 3 wt% for the tests of photocatalytic activity and photoelectrochemistry, while it is controlled to be 10 wt% for the characteristics.

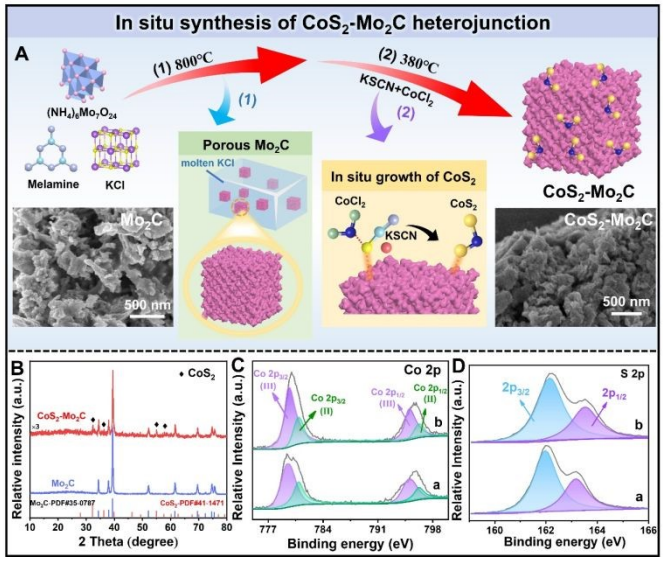

Fig. 2. (A) The schematic diagram for the fabrication of the CoS_2-Mo_2C heterojunction: (1) synthesis of porous Mo_2C and its SEM image and (2) CoS_2 in-situ growth on Mo_2C and the corresponding SEM image; (B) XRD patterns of Mo_2C and CoS_2-Mo_2C(20 wt%); (C-D) The high-resolution XPS spectra of (C) Co 2p and (D) S 2p: (a) CoS_2-Mo_2C(10 wt%) and (b) CoS_2-Mo_2C(20 wt%).

3. Results and discussion

3.1. Synthetic route and characterization of CoS_2-Mo_2C heterojunction cocatalyst

In this work, the CoS_2-Mo_2C heterojunction is synthesized via a two-step calcination approach, including the first production of porous Mo_2C through a KCl salt-template method (Fig. 2A-(1)) and the following in-situ growth of the CoS_2 on the Mo_2C matrix to form the CoS_2-Mo_2C heterojunction (Fig. 2A-(2)). In the initial synthesis step, a homogeneous mixture of ammonium molybdate, melamine, and KCl crystals is calcined at 800 °C during thermal treatment (the melting point of KCl is 770 ℃) while the molten KCl forms a liquid-phase platform to act as a template. After washing with deionized water to remove residual KCl, the final black powder Mo_2C is obtained. The produced Mo_2C (Fig. 2B-a) mainly displays the typical XRD diffraction peaks at 34.7°, 38.1°, and 39.61°, which are in line with the Mo_2C (PDF#35-0787).[48] Besides, the porous structure of the produced Mo_2C crystallites can be strongly confirmed by FESEM analysis (Fig. 2A-Mo_2C). In the subsequent synthesis step, the pre-synthesized Mo_2C with KSCN and $CoCl_2$ is heated at 380 °C to generate the CoS_2-Mo_2C heterojunction, where the KSCN-mediated system forms a homogeneous liquid phase upon melting above 170 °C, followed by thermal decomposition at 380 °C to release active sulfur species. To prove the successful formation of CoS_2-Mo_2C heterojunction, the XRD pattern of the above samples is displayed in Fig. 2B-b. Compared with pure Mo_2C, the CoS_2-Mo_2C shows new diffraction peaks at 32.3°, 36.2°, and 54.9° (CoS_2 JCPDS no. 41-1471) in addition to the corresponding Mo_2C diffraction peak.[49, 50] The in-situ formation of CoS_2 nanoparticles on the Mo_2C matrix yields well-defined heterojunctions with clear interfacial boundaries, as verified by field-emission scanning electron microscopy (Fig. 2A-CoS_2-Mo_2C, FESEM). The successful formation of heterostructure CoS_2-Mo_2C can further be demonstrated via the XPS results. Compared with Co and S peaks in the pure Mo_2C (Fig. S1-a, Supporting Information), new signal peaks corresponding to Co and S elements are observed in the CoS_2-Mo_2C(20 wt%) (Fig. S1-b, Supporting Information). As shown in its high-resolution XPS spectra of Co 2p (Fig. 2C-a), the characteristic peaks at 779.6 eV and 795.0 eV are attributed to Co^{3+} species, while distinct peaks at 780.9 eV and 796.3 eV correspond to Co^{2+} oxidation states.[51] Complementary evidence is observed in the S 2p spectrum (Fig. 2D-a), where the characteristic doublet at 162.0 eV (S $2p_{3/2}$) and 163.2 eV (S $2p_{1/2}$) confirms the successful formation of cobalt sulfide phases in CoS_2-Mo_2C.[52] When the amount of CoS_2 increased from 10 wt% to 20 wt%, the peak area of the XPS characteristic peaks of Co 2p (Fig. 2C-b) and S 2p (Fig. 2D-b) slightly increase. Therefore, the combined XRD, FESEM, and XPS provide conclusive evidence for the successful formation of CoS_2-Mo_2C heterojunctions through this facile calcination approach.

3.2. Preparation and microstructures of CoS_2-Mo_2C/TiO_2 photocatalyst

To further prepare the heterostructured CoS_2-Mo_2C-decorated TiO_2 samples (CoS_2-Mo_2C/TiO_2), pre-synthesized CoS_2-Mo_2C powder undergoes ultrasonic dispersion in a white TiO_2 nanoparticle suspension, as illustrated in Fig. 3A. The resulting homogeneous dark-gray suspension demonstrates uniform integration between the black CoS_2-Mo_2C powder and white TiO_2 nanoparticles. After aging for 5 min, a gray-black precipitate forms at the bottom of the cuvette, and the clear liquid above is colorless (Fig. S2, Supporting Information), providing direct visual evidence for the strong interfacial coupling between the CoS_2-Mo_2C cocatalyst and TiO_2 photocatalyst.[53] To investigate the microstructure of the CoS_2-Mo_2C

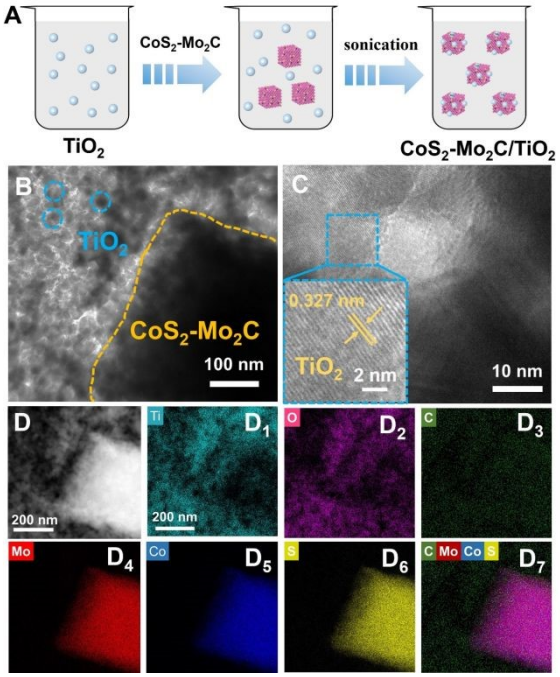

Fig. 3. (A) Schematic diagram for the fabrication of CoS_2-Mo_2C/TiO_2 photocatalyst; (B-C) TEM images, (D) HAADF-STEM, and (D_1-D_7) elemental mapping images of CoS_2-Mo_2C(20 wt%)/TiO_2.

cocatalyst-loaded TiO_2, TEM imaging, and elemental mapping are performed. High-resolution TEM analysis reveals uniformly dispersed spherical nanoparticles (20-50 nm) surrounding the CoS_2-Mo_2C matrix (Fig. 3B), with measured lattice fringes of 0.327 nm corresponding to the (110) crystallographic plane of TiO_2 (Fig. 3C). In this case, the morphology of CoS_2-Mo_2C should be consistent with that observed in the SEM images (seen in Fig. 2) since the ultrasonic method has almost no effect on its structure. Additionally, elemental mapping (Fig. 3D-D7) results confirm the presence of Mo, C, Co, S, Ti, and O, providing strong evidence for the formation of the CoS_2-Mo_2C/TiO_2 composite. Hence, these comprehensive characterizations demonstrate strong interfacial binding between CoS_2-Mo_2C and TiO_2, confirming the high quality of the composite material.

The successful synthesis of the CoS_2-Mo_2C/TiO_2 composite is further confirmed through a comprehensive suite of characterization techniques, including XRD, UV-vis absorption spectra, and XPS. The blank TiO_2 (Fig. 4A-a) displays the typical diffraction peaks of the anatase phase (PDF#21-1272) and rutile phase (PDF#21-1276), which are indicative of its crystalline structure.[51,54] Upon loading the cocatalysts, both Mo_2C/TiO_2 (Fig. 4A-b) and CoS_2-Mo_2C/TiO_2 samples (Fig. 4A-c and d) exhibit well-defined TiO_2 characteristic peaks, demonstrating that the incorporation of Mo_2C and CoS_2-Mo_2C introduces minimal structural modification to the TiO_2 framework. Compared to pristine TiO_2, the XRD patterns of both Mo_2C/TiO_2 and CoS_2-Mo_2C/TiO_2 samples

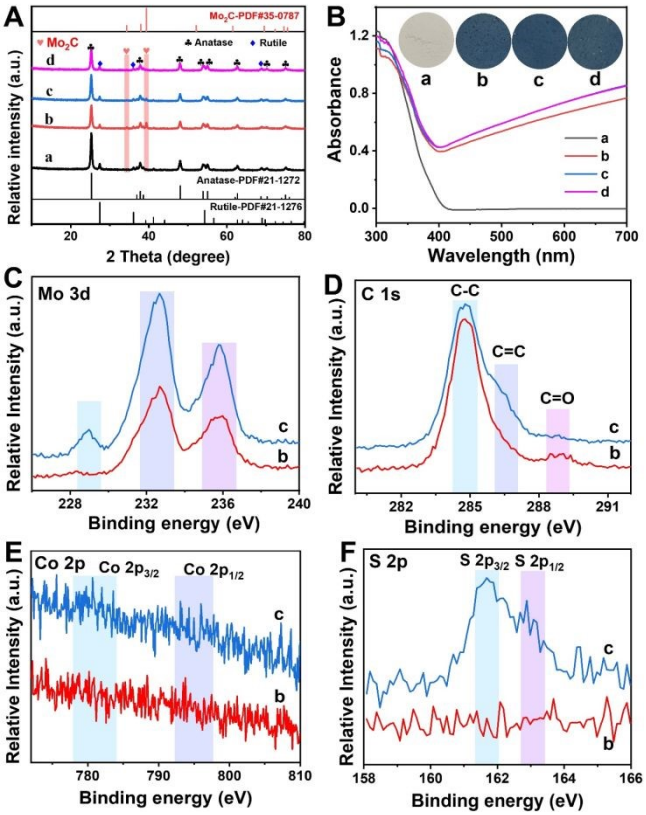

Fig. 4. (A) XRD patterns, (B) UV-vis adsorption spectra, (C-F) XPS survey spectra and high-resolution XPS spectra of (C) Mo 3d, (D) C 1s, (E) Co 2p, and (F) S 2p for various samples: (a) TiO_2, (b) Mo_2C/TiO_2, (c) CoS_2-Mo_2C(10 wt%)/TiO_2, and (d) CoS_2-Mo_2C(20 wt%)/TiO_2.

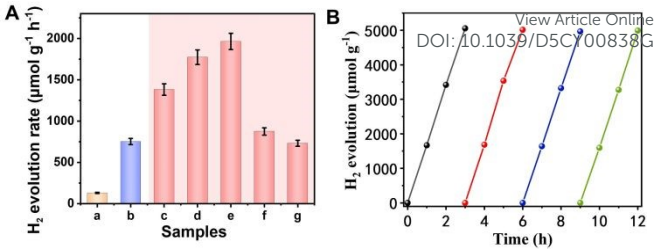

Fig. 5. (A) Photocatalytic H_2-generation rate of (a) TiO_2, (b) Mo_2C/TiO_2, (c) CoS_2-Mo_2C(2 wt%)/TiO_2, (d) CoS_2-Mo_2C(6 wt%)/TiO_2, (e) CoS_2-Mo_2C(10 wt%)/TiO_2, (f) CoS_2-Mo_2C(16 wt%)/TiO_2, and (g) CoS_2-Mo_2C(20 wt%)/TiO_2; (B) The cycling runs of the photocatalytic H_2-evolution activity of CoS_2-Mo_2C(10 wt%)/TiO_2.

display two additional diffraction peaks at approximately 34.7° and 39.6°, which are attributed to Mo_2C, confirming the successful deposition of Mo_2C on the TiO_2 surface. Additionally, this inverse correlation between CoS_2 incorporation and Mo_2C signal attenuation confirms both the controlled compositional adjustment and successful formation of CoS_2-Mo_2C/TiO_2 heterostructures. However, no distinct CoS_2 diffraction peak in the XRD pattern of the CoS_2-Mo_2C/TiO_2 composite appears, which is attributable to its low loading amount. In addition, UV-vis absorption spectra characterize the optical absorption properties of the synthesized samples. The absorption edge of bare TiO_2 (Fig. 4B-a) is around 390 nm, corresponding to a band gap of 3.38 eV as determined by Kubelka-Munk function [55] (Fig. S3). Through proper modulation of the cocatalysts (Mo_2C and CoS_2-Mo_2C), the resulting photocatalysts (Fig. 4B-b, c, and d) showed obvious absorption edges similar to TiO_2(Fig. 4B-a), and the absorption in the visible light region between 400 and 700 nm was significantly stronger than that of pure TiO_2.[56, 57] Besides, the increased visible-light absorption of various photocatalysts can also be demonstrated through their photographs, indicating that the cocatalysts (Mo_2C and CoS_2-Mo_2C) have been efficiently loaded onto the TiO_2 surface. To meticulously uncover the chemical states of surface elements in photocatalysts, XPS survey spectra (Fig. S3-a) and the high-resolution spectra (Fig. 4C-F) are meticulously tested. In addition to Ti and O peaks (Fig. S4A, B, and C), Mo 3dand C 1s XPS signals for Mo_2C materials are clearly displayed in the Mo_2C/TiO_2 sample. The high-resolution Mo 3d spectrum (Fig. 4C-b) shows three distinct peaks at 228.9 eV, 232.7 eV and 235.8 eV, while the C 1s spectrum (Fig. 4D-b) exhibits three components at 284.8 eV (C-C), 286.4 eV (C=C) and 288.8 eV (C=O), confirming the successful synthesis of Mo_2C/TiO_2.[36] Compared with Mo_2C/TiO_2, the CoS_2-Mo_2C/TiO_2 composite additionally contains Co and S elements (Fig. 4E-F). The above research indicates that the CoS_2-Mo_2C/TiO_2 composite photocatalysts can be successfully synthesized through the ultrasonic-assisted synthesis strategy.

3.3. Photocatalytic H_2-generation performance and mechanism of CoS_2-Mo_2C/TiO_2

The photocatalytic H_2-production activities of the photocatalysts are evaluated under visible light irradiation (λ = 365 nm). To investigate the effect of reaction conditions on photocatalytic performance, the H_2-evolution activity of the photocatalysts is evaluated under various sacrificial agents (10 vol% lactic acid, 25

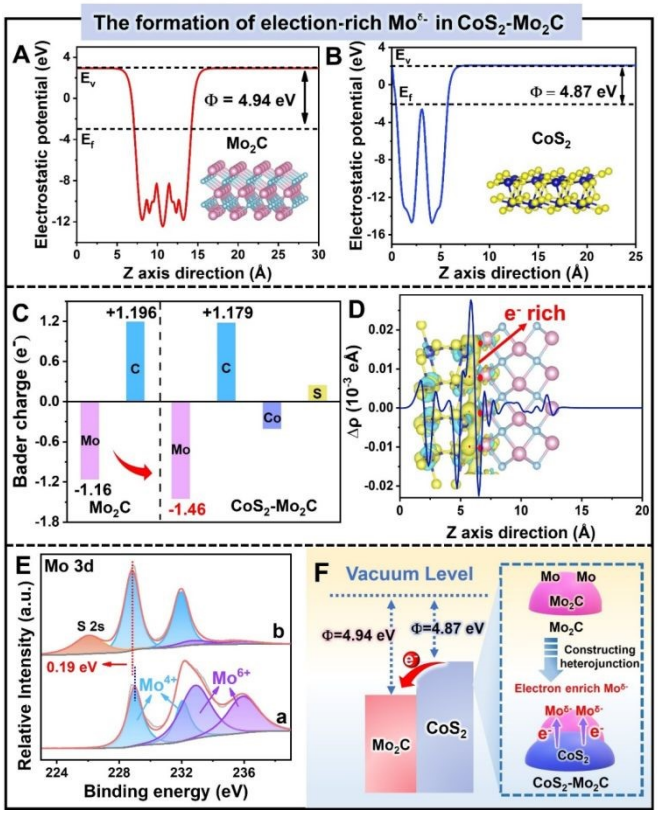

Fig. 6. (A-B) The calculated work function of CoS_2 and Mo_2C; (C) Bader charge calculations of Mo_2C and CoS_2-Mo_2C; (D) The corresponding planar-averaged electron density difference Δρ(z) of CoS_2-Mo_2C; (E) The high-resolution XPS spectra of Mo 3d for (a) Mo_2C and (b) CoS_2-Mo_2C(10 wt%); (F) Graphic diagram for the free-electron migration through the induction of work function difference between CoS_2 and Mo_2C.

vol% ethanol, and 10 vol% TEOA) and ethanol solution (25 vol %) at different pH values (1, 3, 5, 7, 9, and 11). The results are presented in Fig. S5A and S5B. Herein, the CoS_2-Mo_2C(10 wt%)/TiO_2 photocatalyst exhibited the highest hydrogen production rate at pH in 25 vol% ethanol solution. Therefore, all subsequent experiments were performed under these optimized conditions. The pure TiO_2 exhibits a relatively poor H_2-production performance of 130.43 μmol g^{-1} h^{-1} (Fig. 5A-a). When TiO_2 is coupled with Mo_2C, the H_2-evolution performance of Mo_2C/TiO_2 (Fig. 5A-b) significantly improves to 753.09 μmol g^{-1} h^{-1}. The incorporation of CoS_2-Mo_2C heterojunction cocatalysts further enhances the photocatalytic activity of all CoS_2-Mo_2C/TiO_2 composites. When the CoS_2 content is optimized to constitute 10% of the mass fraction of Mo_2C, the resultant CoS_2-Mo_2C(10 wt%)/TiO_2 sample (Fig. 5A-e) achieves a remarkable H_2-evolution rate of 1964.53 μmol g^{-1} h^{-1}, with an apparent quantum efficiency (AQE) of 14.65% (Table S1, Supporting Information), which is 15.10 and 2.60 folds higher than that of pure TiO_2 and Mo_2C/TiO_2, respectively, highlighting the substantial improvement in photocatalytic performance brought about by the CoS_2-Mo_2C cocatalyst. The H_2-production rate of the CoS_2-Mo_2C/TiO_2 photocatalyst is superior to the majority of Mo_2C-based photocatalysts (Table S2). The hydrogen-evolution performance gradually decreases for CoS_2-Mo_2C(16wt%)/TiO_2 (Fig. 5A-f) and CoS_2-Mo_2C(20wt%)/TiO_2 (Fig. 5A-g) samples with increasing CoS_2 content, likely due to enhanced photocorrosion under illumination that adversely affects the catalytic activity. After conducting the cyclic tests, the performance of CoS_2-Mo_2C(10wt%)/TiO_2 also showed relative stability (Fig. 5B). To further investigate the stability of the CoS_2-Mo_2C/TiO_2 photocatalyst, the exceptional stability is confirmed by UV-vis analysis showing negligible differences between before and after illumination spectra (Fig. S6). Therefore, compared with pure TiO_2 and Mo_2C/TiO_2, the CoS_2-Mo_2C/TiO_2 photocatalyst formed by introducing the CoS_2-Mo_2C heterojunction has a higher hydrogen production performance.

The aforementioned hydrogen-generation results demonstrate that the photocatalytic performance of TiO_2 can be significantly enhanced through the integration of CoS_2-Mo_2C. To thoroughly understand the impact of the CoS_2-Mo_2C cocatalyst, both Density Functional Theory (DFT) calculations and XPS data are employed to investigate its electronic configuration and the underlying mechanism. Based on the constructed slab models of CoS_2 and Mo_2C structures (Fig. S7), the work functions (Φ) of Mo_2C and CoS_2 are calculated to be 4.94 eV and 4.87 eV, respectively (Fig. 6A and B). The work function difference

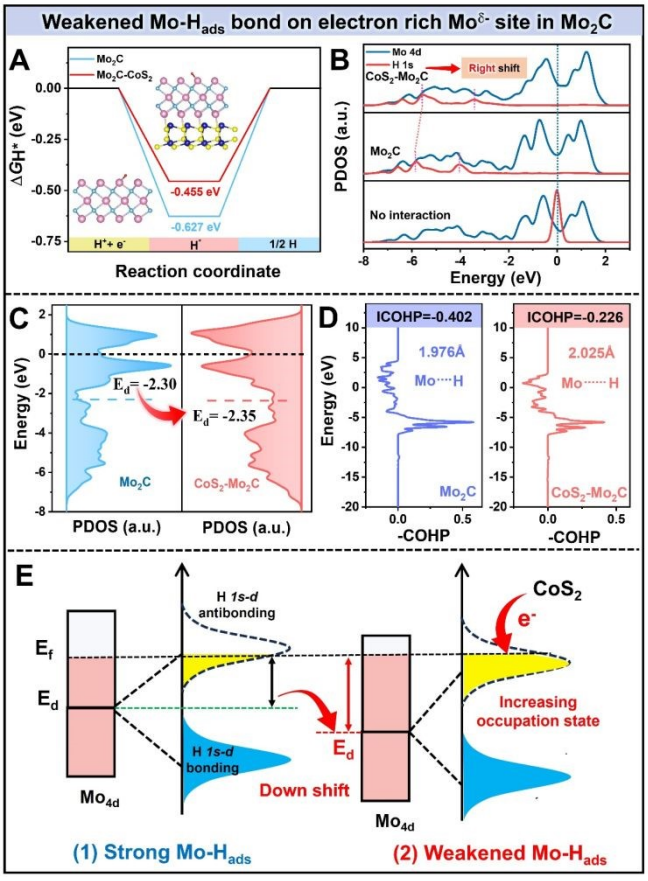

Fig. 7. (A) Gibbs free energy profiles (ΔG_{H^*}) for H_{ads} on different sites; (B-C) PDOS and (D) COHP analyses of the H adsorption on Mo_2C and CoS_2-Mo_2C; (E) Corresponding d band center of Mo 3d for Mo_2C and CoS_2-Mo_2C.

between CoS_2 and Mo_2C drives interfacial electron transfer upon heterojunction formation, with electrons spontaneously migrating from the lower-work-function CoS_2 to the higher-work-function Mo_2C component.[58] This appropriate difference in work function is conducive to electron transfer. To further substantiate these findings, Bader charge calculations (Fig. 6C) substantiate the increased electron density of Mo atoms (from -1.16 to -1.46) in the CoS_2-Mo_2C structure, confirming the formation of electron-enriched $Mo^{\delta-}$ active sites through interfacial charge redistribution. At the same time, the charge density difference analysis of CoS_2-Mo_2C (Fig. 6D) reveals electron accumulation predominantly on Mo_2C and positive charge distribution around CoS_2 regions, demonstrating electron transfer from CoS_2 to Mo_2C that generates electron-enriched Mo active sites. The XPS spectra demonstrate a 0.19 eV negative binding energy shift for Mo 3d orbitals in CoS_2-Mo_2C (Fig. 6E-b) relative to pristine Mo_2C (Fig. 6E-a), providing spectroscopic confirmation of electron accumulation at Mo sites.[47] This electron enrichment effect extends to the carbon matrix, as evidenced by a 0.12 eV reduction in the C 1s binding energy (Fig. S8). Thus, the combined computational analysis (work function, Bader charge, and charge density difference) and XPS results conclusively demonstrate that the CoS_2-Mo_2C structure induces charge density redistribution, leading to the formation of electron-enriched $Mo^{\delta-}$ sites (Fig. 6F).

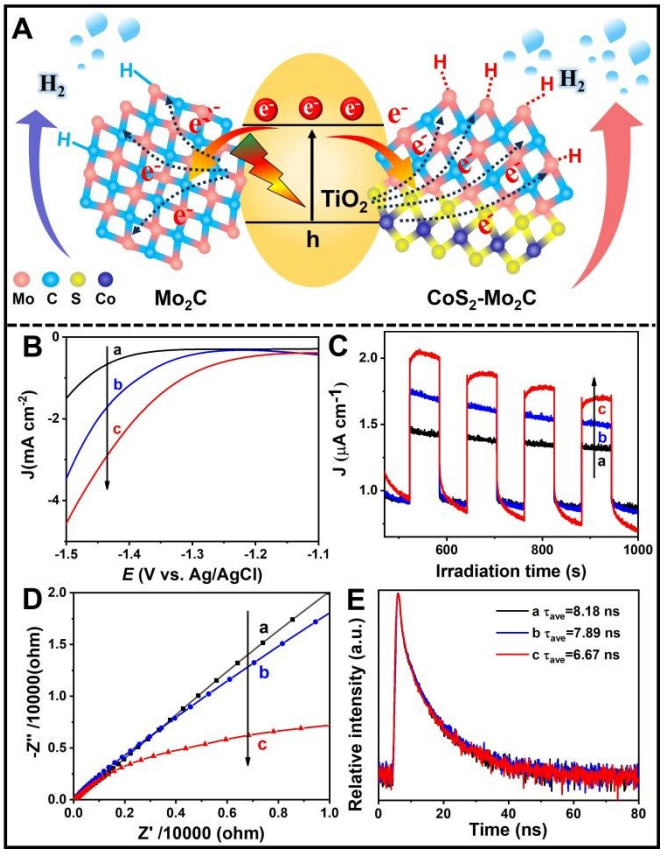

Fig. 8. (A) The photocatalytic hydrogen-generation mechanism of Mo_2C modified-TiO_2 and (b) CoS_2-Mo_2C modified-TiO_2. (B) Linear sweep voltammetry (LSV) curves, (C) transient-state photocurrent (i-t) spectra, (D) electrochemical impedance spectra (EIS), and (E) transient-state photoluminescence spectra of (a) TiO_2, (b) Mo_2C/TiO_2, and (c) CoS_2-Mo_2C(10 wt%)/TiO_2.

To elucidate the influence of electron-enriched Mo site on Mo-H_{ads} bond strength and the underlying mechanism, theoretical calculations including hydrogen adsorption free energy (ΔG_{H^*}), density of states (PDOS and TDOS), and crystal orbital Hamiltonian population (COHP) are systematically performed (Fig. 7A-C and S9). As illustrated in Fig. 7A, the hydrogen adsorption free energy (ΔG_{H^*}) of pristine Mo_2C measures -0.627 eV (Figure 7A), indicating strong chemical bonding between the Mo site and adsorbed hydrogen atom. When the CoS_2-Mo_2C heterojunction is formed, the binding of Mo site in the CoS_2-Mo_2C structure with hydrogen shows a more moderate ΔG_{H^*} value (-0.423 eV). The observed ΔG_{H^*} shift confirms that electron accumulation at $Mo^{\delta-}$ site in the CoS_2-Mo_2C heterostructure effectively reduces Mo-H_{ads} bond strength. In fact, the aforementioned findings can be further corroborated by the subsequent projected density of states (PDOS) and integrated crystal orbital Hamilton population (ICOHP) analyses. As depicted in Fig. 7B-Mo_2C, when hydrogen interacts with the Mo site, the resulting s-d hybridization orbitals shift downward relative to the Fermi level, indicating that hydrogen can adsorb onto Mo atoms to form Mo-H_{ads} bond. In this context, compared to Mo_2C, the s-d hybridization orbital energies of Mo-H_{ads} in CoS_2-Mo_2C (Fig. 7B-Mo_2C) are elevated (shifted to the right), indicating that the adsorption of hydrogen at the Mo site in CoS_2-Mo_2C has weakened. Moreover, the d-band center (E_d) theory offers a comprehensive explanation for the weakened Mo-H_{ads} bond. Upon forming the CoS_2-Mo_2C heterojunction and facilitating free electron transfer, as illustrated in Fig. 7C, the E_d of Mo 4d in CoS_2-Mo_2C (-2.35 eV) shifts lower than that of Mo_2C (-2.30 eV). This shift increases the antibonding-orbital occupancy and consequently weakens the Mo-H_{ads} bond. The ICOHP analysis shows a significantly higher value for CoS_2-Mo_2C (-0.226, Fig. 7D-CoS_2-Mo_2C) compared to pristine Mo_2C (-0.402, Fig. 7D-Mo_2C), with the increased ICOHP enhancing antibonding-orbital occupancy and consequently weakening the Mo-H_{ads} bond strength.[59] Meanwhile, the CoS_2-Mo_2C exhibits a more unstable Mo-H_{ads} bond (bond length is 2.025 Å) compared to the single Mo_2C (bond length is 1.976 Å). Therefore, the aforementioned results conclusively demonstrate that the formation of CoS_2-Mo_2C heterojunctions enhances the antibonding-orbital occupancy of Mo active centers, thereby decreasing the intensity of Mo-H_{ads} bond and facilitating the rapid interfacial H_2 production reaction (Fig. 7E).

The hydrogen-evolution performance confirms the effectiveness of the prepared CoS_2-Mo_2C composite as a cocatalyst for significantly enhancing TiO_2 photocatalytic activity, with the proposed dual mechanisms (Fig. 8A) elucidating the distinct hydrogen production pathways between Mo_2C/TiO_2 (Fig. 8A-left) and CoS_2-Mo_2C/TiO_2 (Fig.8A-right) systems. In traditional Mo_2C modified TiO_2 photocatalysts, under the irradiation of UV light, the photogenerated electrons from TiO_2 are excited and subsequently migrate to Mo_2C cocatalyst, thereby promoting interfacial hydrogen-generation reaction. The formation of CoS_2-Mo_2C heterojunctions facilitates rapid electron transfer from TiO_2 to Mo_2C, generating additional electron-enriched $Mo^{\delta-}$ sites that weaken Mo-H_{ads} bond and consequently enhance interfacial hydrogen evolution. The photocatalytic mechanism of CoS_2-

Mo_2C/TiO_2 is further elucidated through comprehensive photoelectrochemical measurements and time-resolved photoluminescence (TRPL) spectroscopy (Fig. 8B-E). To evaluate its impact on H_2 evolution, linear sweep voltammetry (LSV) is performed on TiO_2, Mo_2C/TiO_2, and CoS_2-Mo_2C/TiO_2 (Fig. 8B). Notably, CoS_2-Mo_2C/TiO_2 exhibits the highest cathodic current, confirming a greater density of active sites for the H_2-evolution reaction. Additionally, CoS_2-Mo_2C/TiO_2 demonstrates a substantially higher instantaneous photocurrent density (Fig. 8C) and a smaller electrochemical impedance spectroscopy (EIS) arc radius (Fig. 8D) compared to TiO_2 and Mo_2C/TiO_2, indicating more efficient charge separation and transfer.[60-63] Furthermore, TRPL analysis (Fig. 8E and Table S3, Supporting Information) reveals that CoS_2-Mo_2C/TiO_2 has an average fluorescence lifetime (τ_{ave}) of 6.67 ns, shorter than those of Mo_2C/TiO_2 (7.89 ns) and TiO_2 (8.18 ns). This reduced lifetime suggests that CoS_2-Mo_2C effectively suppresses electron-hole recombination.[64,65] Hence, CoS_2-Mo_2C not only accelerates electron transfer but also introduces additional catalytic active sites, optimizing interfacial hydrogen evolution and substantially boosting the photocatalytic performance of TiO_2. Furthermore, it is of great significance to explore the application of the CoS_2-Mo_2C heterojunction in visible-light-driven CdS. Compared with pure CdS, CoS_2-Mo_2C(10 wt%)/CdS by the similar ultrasonic dispersion method to CoS_2-Mo_2C(10 wt%)/TiO_2 exhibits enhanced activity (Fig. S10), indicating that CoS_2-Mo_2C is a multifunctional auxiliary catalyst that improves the hydrogen generation efficiency of the photocatalyst.

4. Conclusions

In summary, this study successfully implements an electronic transfer strategy that weakens the Mo-H_{ads} bond by increasing antibonding orbital occupancy through the construction of CoS_2-Mo_2C heterojunction. The CoS_2-Mo_2C heterojunction cocatalyst is synthesized via the two-step calcination method and then integrated with TiO_2 through the ultrasonic-assisted strategy to form the CoS_2-Mo_2C/TiO_2 photocatalyst. Photocatalytic hydrogen-evolution tests reveal that the CoS_2-Mo_2C (10 wt%)/TiO_2 sample achieves an exceptional hydrogen production rate of 1964.53 μmol h^{-1} g^{-1}, representing 15.10-fold and 2.60-fold enhancements compared to pristine TiO_2 and Mo_2C/TiO_2, respectively. Theoretical calculations and experimental evidence consistently confirm that the antibonding orbital occupancy at Mo sites increases by the electron transfer from CoS_2 to Mo_2C in the CoS_2-Mo_2C heterojunction, leading to the weakened Mo-H_{ads} bond from 1.976 Å in Mo_2C to 2.025 Å in CoS_2-Mo_2C for consequently enhanced photocatalytic efficiency of TiO_2. This work establishes a promising strategy for optimizing the photocatalytic performance of Mo_2C-based photocatalysts through the heterojunction construction.

Author Contributions

Youran Xia: Methodology, Validation, Writing original draft, and Data curation; Ping Wang: Conceptualization, Data curation, Supervision, Resources, Project administration, Funding acquisition, and Writing-review & editing; Feng Chen: Software; Xuefei Wang: Data analysis and Writing-review & editing; Huogen Yu: Conceptualization, Data curation, Supervision, and Funding acquisition.

Conflicts of interest

There are no conflicts to declare.

Acknowledgements

This work was supported by the National Natural Science Foundation of China (22178275, 22472127, and U22A20147) and the Natural Science Foundation of Hubei Province of China (2022CFA001).

References

1. Z. Qi, J. Chen, Q. Li, N. Wang, S. A. C. Carabineiro and K. Lv, *Small*, 2023, **19**, 2303318.
2. Z. Yu, C. Guan, X. Yue and Q. Xiang, *Chin. J. Catal.*, 2023, **50**, 361-371.
3. J. Wang, Y. Zhang, S. Jiang, C. Sun and S. Song, *Angew. Chem. Int. Ed.*, 2023, **62**, e202307808.
4. Y. Hu, X. Yu, Q. Liu, L. Wang and H. Tang, *Carbon*, 2022, **188**, 70-80.
5. Z. Wang, B. Su, J. Xu, Y. Hou and Z. Ding, *Int. J. Hydrogen Energy*, 2020, **45**, 4113-4121.
6. M. Zhao, S. Liu, D. Chen, S. Zhang, S. A. C. Carabineiro and K. Lv, *Chin. J. Catal.*, 2022, **43**, 2615-2624.
7. X. Wu, J. Zhou, Q. Tan, K. Li, Q. Li, S. A. Correia Carabineiro and K. Lv, *ACS Appl. Mater. Interfaces*, 2024, **16**, 11479-11488.
8. X. Fu, H. Huang, G. Tang, J. Zhang, J. Sheng and H. Tang, *Chin. J. Struct. Chem.*, 2024, **43**, 100214.
9. Z. Yu, F. Li and Q. Xiang, *J. Mater. Sci. Technol.*, 2024, **175**, 244-257.
10. Z. Chen, P. Wang, X. Wang and H. Yu, *Surf. Interfaces*, 2024, **51**, 104684.
11. J. Li, Y. Li, X. Wang, Z. Yang and G. Zhang, *Chin. J. Catal.*, 2023, **51**, 145-156.
12. D. Liu, B. Sun, S. Bai, T. Gao and G. Zhou, *Chin. J. Catal.*, 2023, **50**, 273-283.
13. E. Lu, J. Tao, C. Yang, Y. Hou, J. Zhang, X. Wang, X. Fu, *Acta Phys. -Chim. Sin.*, 2023, **39**, 2211029.
14. Y. Wu, J. Cao, R. Peng, M. Cao, G. Peng, W. Yuan and X. Luo, *Catal. Sci. Technol.*, 2024, **14**, 1579-1587.
15. F. Li, Z. Fang, Z. Xu and Q. Xiang, *Energy Environ. Sci.*, 2024, **17**, 497-509.
16. H. Li, Y. Chen, Q. Niu, X. Wang, Z. Liu, J. Bi, Y. Yu and L. Li, Chin. *J. Catal.*, 2023, **49**, 152-159.
17. K. Khan, Z. U. Rehman, S. Yao, M. Nawaz, M. Orlandi, A. Miotello, M. Ullah, K. Ullah, A. A. Alanazi and M. E. A. Zaki, *Int. J. Hydrogen Energy*, 2024, **80**, 427-434.
18. H. He, Z. Wang, K. Dai, S. Li and J. Zhang, *Chin. J. Catal.*, 2023, **48**, 267-278.
19. L. Xiao, S. Shen, M. Chen, R. Liao, Y. Zhou, X. Li, *Acta Phys. -Chim. Sin.*, 2024, **40**, 2308036.
20. E. Bianco, F. Sordello, F. Pellegrino and V. Maurino, *Catal. Sci. Technol.*, 2024, **14**, 7205-7211.
21. Z. Li, W. Huang, J. Liu, K. Lv and Q. Li, *ACS Catal.*, 2021, **11**, 8510-8520.
22. W. Yang, J. Zhang, Q. Xu, Y. Yang, L. Zhang, *Acta Phys. Chim. Sin.*, 2024, **40**, 2312014.

23. M.-H. Liu and Y. Takahashi, *Catal. Sci. Technol.*, 2024, **14**, 1756-1759.
24. G. Cheng, X. Liu and J. Xiong, *Chem. Eng. J.*, 2024, **501**, 157491.
25. J. Xu, X. Zhang, X. Wang, J. Zhang, J. Yu and H. Yu, *ACS Catal.*, 2024, **14**, 15444-15455.
26. J. Tao, M. Wang, X. Zhang, L. Lu, H. Tang, Q. Liu, S. Lei, G. Qiao and G. Liu, *Appl. Catal. B Environ.*, 2023, **320**, 122004.
27. Y. Wang, S. Jiang, C. Sun and S. Song, *J. Mater. Sci. Technol.*, 2024, **190**, 210-217.
28. A. Sikandaier, Y. Zhu and D. Yang, *Chin. J. Struct. Chem.*, 2024, 43, 100242.
29. H. Zou, M. Pan, P. Wang, F. Chen, X. Wang and H. Yu, *Catal. Sci. Technol.*, 2024, **14**, 5731-5738.
30. T. Zhou, X. Liu, L. Zhao, M. Qiao, W. Lei, *Acta Phys. -Chim. Sin.*, 2024, **40**, 2309020.
31. Q. Shang, H. Wang, C. Kan, R. Ding, Y. Li, S. Pandeya, Z. Li and M. K. Joshi, *Catal. Sci. Technol.*, 2024, **14**, 6833-6844.
32. J. Xia, J. Tian, T. Sun, J. Fan and E. Liu, *Surf. Interfaces*, 2024, **47**, 104218.
33. P. Deng, D. Gao, P. Wang, X. Wang, F. Chen and H. Yu, *J. Mater. Chem. A.*, 2023, **11**, 21874-21883.
34. H. Zhang, Z. Wang, J. Zhang and K. Dai, *Chin. J. Catal.*, 2023, **49**, 42-67.
35. M. Song, X. Song, X. Liu, W. Zhou and P. Huo, *Chin. J. Catal.*, 2023, **51**, 180-192.
36. J. Liu, P. Wang, J. Fan, H. Yu and J. Yu, *ACS Sustain. Chem. Eng.*, 2021, **9**, 3828-3837.
37. J. Wu, P. Qiao, P. An, M. Zhang, H. Xiu, Z. Song, K. Li, Y. Cui, Y. Wang and W. Yao, *Appl. Catal. B Environ. Energy*, 2025, **377**, 125481.
38. L. Gao, J. Liu, H. Long, P. Wang and H. Yu, *Catal. Sci. Technol.*, 2021, **11**, 7307-7315.
39. W. Chen, M. Niu, Z. Zhang, L. Chen, X. Li, J. Zhang, R. Sun, H. Cao and X. Wang, *Small*, 2024, **20**, 2311026.
40. M. Pan, P. Wang, X. Wang, F. Chen and H. Yu, *ACS Sustain. Chem. Eng.*, 2023, **11**, 13222-13231.
41. S. Yuan, M. Xia, Z. Liu, K. Wang, L. Xiang, G. Huang, J. Zhang and N. Li, *Chem. Eng. J.*, 2022, **430**, 132697.
42. Y. Xu, J. Yang, T. Liao, R. Ge, Y. Liu, J. Zhang, Y. Li, M. Zhu, S. Li and W. Li, *Chem. Eng. J.*, 2022, **431**, 134126.
43. R. Liu, P. Wang, X. Wang, F. Chen and H. Yu, *Small*, 2025, **21**, 2408330.
44. S. Wang, S. Zhu, Z. Cui, Z. Li, S. Wu, W. Xu, Z. Gao, Y. Liang and H. Jiang, *J. Mater. Chem. A*., 2025, **13**, 3084-3093.
45. X. Ke, P. Wang, X. Wang, F. Chen and H. Yu, *Appl. Catal. B Environ. Energy*, 2025, **365**, 124936.
46. X. Luo, Q. Zhou, S. Du, J. Li, L. Zhang, K. Lin, H. Li, B. Chen, T. Wu, D. Chen, M. Chang and Y. Liu, *ACS Appl. Mater. Interfaces*, 2018, **10**, 42335-42347.
47. J. Liu, P. Wang, L. Gao, X. Wang and H. Yu, *J. Mater. Chem. C.*, 2022, **10**, 3121-3128.
48. J. Qian, Y. Xing, Y. Yang, Y. Li, K. Yu, W. Li, T. Zhao, Y. Ye, L. Li, F. Wu and R. Chen, *Adv. Mater.*, 2021, **33**, 2100810.
49. N. Zhang, G. Wang, G. Zhang, K. Chen and K. Chu, *Chem. Eng. J.*, 2023, **474**, 145861.
50. Y. Guo, L. Gan, C. Shang, E. Wang and J. Wang, *Adv. Funct. Mater.*, 2017, **27**, 1602699.
51. F. Chen, H.-F. Feng, W. Luo, P. Wang, H.-G. Yu and J.-J. Fan, *Rare Met.*, 2021, **40**, 3125-3134.
52. S. Hussain, S. Aftab, Z. Abbas, I. Hussain, S. F. Shaikh, K. Karuppasamy, H.-S. Kim, J. Jung and D. Vikraman, *Inorg. Chem. Front.*, 2024, **11**, 4001-4018.
53. J. Liu, P. Wang, J. Fan, H. Yu and J. Yu, *Nano Res.*, 2021, **14**, 1095-1102.
54. Q. Liu, J. Huang, H. Tang, X. Yu and J. Shen, *J. Mater. Sci. Technol.*, 2020, **56**, 196-205.
55. P. Lu, B. Du, K. Liu, Z. Luo, A. Sikandaier, L. Diao, J. Sun, L. Jiang and Y. Zhu, *Chin. J. Struct. Chem.*, 2024, **43**, 100361.
56. M. Wang, P. Wang, X. Wang, F. Chen and H. Yu, *J. Mater. Sci. Technol.*, 2024, **174**, 168-175.
57. X. Liu, Y. Zhang, W. Zhang, G. Cheng, F. Tian, W. Li and J. Xiong, *J. Colloid Interface Sci.*, 2025, **685**, 173-185.
58. X.-Q. Qiao, C. Li, W. Chen, H. Guo, D. Hou, B. Sun, Q. Han, C. Sun and D.-S. Li, *Chem. Eng. J.*, 2024, **490**, 151822.
59. R. Liu, P. Wang, X. Wang, F. Chen and H. Yu, *Acta Phys. -Chim. Sin.*, 2025, **41**, 100137.
60. F. Wei, J. Zhao, Y.-C. Liu, Y.-H. Hsu, S.-F. Hung, J. Fu, K. Liu, W. Lin, Z. Yu, L. Tan, X. F. Lu, C. Feng, H. Zhang and S. Wang, *Nat. Commun.*, 2025, **16**, 6586.
61. T. Y. Huang, Z. Yang, S. Y. Yang, Z. H. Dai, Y. J. Liu, J. H. Liao, G. Y. Zhong, Z. J. Xie, Y. P. Fang and S. S. Zhang, *J. Mater. Sci. Technol.*, 2024, **171**, 1-9.
62. X. Zhou, Y. Tian, J. Luo, B. Jin, Z. Wu, X. Ning, L. Zhan, X. Fan, T. Zhou, S. Zhang and X. Zhou, *Adv. Funct. Mater.*, 2022, **32**, 2201518.
63. K. Khan, A. M. Idris, H. Hassan, S. Haider, S. U.-D. Khan, A. Miotello and I. Khan, *Adv. Powder Mater.*, 2025, 4, 100284.
64. B. Su, M. Zheng, W. Lin, X. F. Lu, D. Luan, S. Wang and X. W. Lou, *Adv. Energy Mater.*, 2023, **13**, 2203290.
65. H. Long, X. Zhang, Z. Zhang, J. Zhang, J. Yu and H. Yu, *Nat. Commun.*, 2025, **16**, 946.

View Article Online
DOI: 10.1039/D5CY00838G

All relevant data are within the manuscript and its additional files.